European Journal of Mechanics B/Fluids 36 (2012) 139–151

Contents lists available at SciVerse ScienceDirect

European Journal of Mechanics B/Fluids

journal homepage: www.elsevier.com/locate/ejmflu

Experiments on the two-dimensional flow of a grain–water mixture past a circular cylinder

Sandro Longo [a,*], Alessandro Valiani [b], Luisfilippo Lanza [b]

[a] Department of Civil Engineering, University of Parma, Parco Area delle Scienze, 181/A, 43100 Parma, Italy
[b] Department of Civil Engineering, University of Ferrara, Via Saragat, 1, 44122 Ferrara, Italy

ARTICLE INFO

Article history:
Received 20 October 2011
Received in revised form
16 February 2012
Accepted 2 April 2012
Available online 19 April 2012

Keywords:
Granular mixture
Sediment transport
Experiments

ABSTRACT

We present experiments with a mixture of grains and water around a circular cylinder. Flow is driven by the internal cylinder of a Taylor–Couette cell. Velocity measurements of the mixture at the external surface are carried out using a commercial particle image velocimeter. The flow regime is in the macroviscous range and the flow field is similar to that generated by a Newtonian fluid around a circular cylinder, with a wake and a recirculation zone. Like in other granular flows, the velocity covariance tensor and the rate of deformation tensor are not collinear; they have principal axes rotated nearly 45°. Near the body, the velocity scale of the wake decays linearly at high Reynolds numbers and logarithmically at low Reynolds numbers. The transverse length scale increases as x'^{n} (x' measured along the axis of symmetry with the origin at the boundary of the body) with $n < 0.5$ (or nearly zero in some flow conditions).

1. Introduction

The analysis of granular flow in the presence of an obstacle is of interest from a theoretical point of view as a study of the complex rheology of a fluid as well as for other applications. Many defence structures against debris flow consist of steel sheeting cylinder piles filled with local materials and capped with concrete. These dissipate the flow energy, stopping boulders, and favouring water filtration. Other defence structures against snow avalanches have a triangular shape with a pyramidal elevation, with a corner in the expected flow direction; these can protect the buildings in their wakes. There are also many applications in food manufacturing, chemistry, and pharmacy. Despite this, experiments and theoretical models are rare.

The flow of a fluid–granular mixture is characterized by three main regimes: (i) a macroviscous regime with essentially Newtonian behaviour, (ii) a dilatant regime with interparticle collisions dominant, and (iii) a quasi-static regime, with stresses transferred mainly as frictional stresses. The complicated structure of the flow field can be better analyzed by reducing the flow to two dimensions. Specific interest has been devoted to analyzing the drags on obstacles in a granular medium. The drag shows that a different behaviour is expected if the obstacles are moving in a granular medium at rest or if the obstacles are at rest and are invested by a granular stream. In both cases, the presence of grains at high concentrations near the obstacles induces stress transmission through contact forces and leads to a jammed state. This jammed state is peculiar of granular flows, different with respect to classical Newtonian fluid flows. Jamming can be induced by gravity for particles at the contact subject to their own weight, or it can be a consequence of any compressive stress. The main kinematic effect of jamming is the need for a proper reorganization of the flow pattern around obstacles dragged in a granular medium. The length scale of the reorganization pattern is different in the two extreme situations, and generally strongly enhances the disturbances induced by the obstacles, favouring strong fluctuations of the drag force. If the granular medium is at rest (on average), the drag usually depends little on the speed or on the form of its cross-section [1], at least if a dry granular flow with a free surface is present. It appears that the influence of speed on drag is important only at low velocities. If the obstacle is at rest, a much stronger dependence on granular velocity is expected, with a low resistance similar to that for a usual fluid (a quadratic law at high velocities). In addition, these results can be strongly different if a lubricant interstitial fluid is present. Some numerical experiments on the interaction of a stream of granular particles with a resting obstacle in two dimensions [2] show that, at low velocities, the drag depends on a 3/2 power of the velocity, whereas, at high velocities, the drag recovers its usual quadratic dependence.

Numerical simulation is also used for studying granular flows. Wassgren et al. [3] used discrete element simulations to investigate a two-dimensional dilute dry granular flow around an immersed cylinder (no interparticle fluid) in order to evaluate the drag

* Corresponding author. Tel.: +39 0521 905157; fax: +39 0521905924.
E-mail address: sandro.longo@unipr.it (S. Longo).

0997-7546/$ – see front matter © 2012 Elsevier Masson SAS. All rights reserved.
doi:10.1016/j.euromechflu.2012.04.002

Nomenclature

$\overline{\dots}$	Time-average operator
$\widetilde{\dots}$	Non-dimensional operator
α, β	Coefficients
δ	Thickness of the gap
γ	Turbulence index
Γ	Shear rate
ϕ, ϕ_D, ϕ_B	Angle of the principal axes of the velocity covariance tensor, of the rate of deformation tensor, of the kinetic stress tensor
Λ_{ij_k}, λ_{ij_k}	Integral length scale, Taylor micro scale corresponding to the correlation between the velocity components i and j in direction x_k
λ	Linear concentration of the solid phase, Taylor microscale
μ	Dynamic fluid viscosity
ν_{mixture}	Kinematic viscosity of the mixture
ρ	Bulk density of the solid phase
ρ_s	Mass density of the solid phase
σ_{kx}, σ_{ky}	Kinetic normal stress along x, y
τ_{kxy}	Kinetic tangential stress
ω, ω_z	Rotation rate, vorticity component along z
a, b, a_1, b_1, c_1, d_1, e_1, a_2, b_2, c_2, d_2, e_2	Coefficients
Ba	Bagnold number
C, C_0	Void concentration of the grains (ratio between the volume of sediments and the bulk volume), maximum void concentration of the grains
d	Grain diameter
D	Diameter of the cylinder
f	Frequency of shedding of the von Karman vortices
l	Transverse length scale, mean free path of the particles
L	Length of the recirculating zone
$L_{x,y}(\dots)$	Polynomials for spatial correction along x, y
LDA	Laser Doppler anemometry
n	Exponent
PIV	Particle image velocimetry
PMMA	Polymethyl methacrylate
R_{ij}	Correlation function between velocity components i and j
Re, Re_Λ	Reynolds number, based on integral scale
R^2	Coefficient of determination
St	Strouhal number
s	Wall thickness
t, dt	Time, time increment
T	Granular temperature
U_0	Reference asymptotic velocity
U_s	Defect velocity
U_x, U_y	Horizontal, vertical instantaneous velocity
U'_x, U'_y	Horizontal, vertical fluctuating velocity
x, x', y	Spatial coordinates
x_{corr}, x_{meas}, y_{corr}, y_{meas}	Spatial coordinates measured, corrected

coefficient. They found that the drag coefficient depends on the Mach number, expressed as the ratio of the asymptotic velocity and the celerity of sound, and on the Knudsen number, expressed as the ratio between the mean free path of the upstream particles and the macroscopic length scale, assumed equal to the diameter of the cylinder. They also depicted some properties of the granular flow, including velocity, temperature, and the solid fraction field. Chehata et al. [4] experimentally studied the flow around a fixed cylinder immersed in a uniform dry and dense granular flow. They found that the drag force is independent of the mean flow velocity and that it scales with the asymptotic stress state in a tall granular bed. They also analyzed the vorticity and the granular temperature field.

Compared to other flows, granular flows are often characterized by variations in bulk density. Experiments by Gray et al. [5] show that a granular stream impacting an obstacle or being deviated by a wall has different zones of compression and expansion with shocks and discontinuities. In these experiments, it is very difficult to measure the fluid velocity in the body stream. It is possible to use laser Doppler anemometry (LDA) [6] and particle image velocimetry (PIV) [7] for measuring velocities near a transparent wall. While PIV exactly displays the particle motion, results usually underestimate the real velocity due to the wall boundary layer (unless it is used for measuring a free granular surface), but, fortunately, this error is limited due to slip of granular flows at the boundary.

The literature includes several references on Newtonian fluid flows around a circular cylinder (see [8]), and most elementary theory of infinite length wings uses conformal mapping of flow around a circular cylinder of infinite extent. Sarpkaya et al. [9] present a detailed analysis on the flow of water and polymer additive around a circular cylinder. The most obvious effect of the additives is instability of the separation curve of the stream, due exclusively to the rheology of the fluid. Nedderman et al. [10] analyze the gravity-driven flow of mustard seeds around a cylinder, adopting a kinematic description based on a stochastic model. Other more detailed analyses refer to the kinematics of complex fluids around bodies [11].

We observe that several models have been developed and tested for dry grain rapid granular flows, mainly based on the assumption of an isotropic granular temperature, small dissipation and low to mid grain void concentration. Significant progress has also been made regarding granular temperature anisotropy. However, little has been done to include the effects of interstitial fluid since Bagnold's pioneering work [12]. Bagnold was interested in the rheology of the mixture, without considering the interaction with a solid boundary except for momentum transferring, and developed a model widely used for its simplicity that makes it an excellent tool for practical computations or simplified models. The flow field in Bagnold's experimental apparatus was viscometric as much as possible. Despite several critics [13], and despite the limitations of the model (e.g., the evidence that it does not develop a constitutive equation, lacking, for example, a tensorial formulation), Bagnold's model is still adopted at least for concentrated suspensions of grains in water at low shear rates (Bagnold's macroviscous regime).

2. Scope and objectives

The aim of the present experimental work is to provide information on the kinematics of flow fields past a cylinder immersed in a fluid–granular mixture stream with grains at high void concentrations. Compared to most experiments in the literature, the presence of water as the interparticle fluid represents a significant variation, producing different results. Such mixtures are common in environmental flows, such as debris flows, but also in industry, as fluidized beds for chemical reactions. The device used to generate the stream is a Taylor–Couette cell; momentum is transferred from the internal rotating cylinder through collisions with the grains of the mixture and through a (limited) wall stress acting on the fluid phase. The device is easy to control and does not suffer many of the limitations typical of channels with recirculating mixture, such as varying void concentration of the grains and free surface instabilities. The use of almost neutrally buoyant grains limits gravity effects that would induce a normal stress increase

with depth. Note that gravity, which acts as a source of momentum in a gravity channel, is a disturbing effect in this device, because it favours particle segregation and grain void increments downward. The source of momentum is a surface force exerted on the internal boundary of the fluid domain, essentially on grains and, to a lesser degree, the interparticle fluid.

In Section 2, we describe the experimental set-up, the measurement technique, and the tests carried out with a mixture of sediments and water. In Section 3 we describe the experimental set-up and the experiments.

In Section 4 we describe the flow field using the experimental data, with an analysis of the wake, the vorticity field, and the divergence of the flow. Conclusions are reported in the last section.

3. Methodology

3.1. Experimental set-up

Experiments were performed in a concentric-cylinder Taylor–Couette shear cell (Fig. 1), with an internal rotating vertical cylinder of stainless steel with a diameter $D_{\text{int}} = 167$ mm and an external fixed cylinder of polymethyl methacrylate (PMMA) with a diameter $D_{\text{ext}} = 190$ mm. The height of the cell is 340 mm, the wall thickness of the external fixed cylinder is $s = 5$ mm, and the annular gap between cylinders, representing the shear section, is $\delta = 11.5$ mm. The internal cylinder is in motion, and in order to transfer momentum to the granular mixture, its wall is roughed by gluing sandpaper to it. The sandpaper has a roughness comparable with the size of the grains; its overall thickness is less than 1 mm.

The internal surface of the PMMA cylinder is smooth, and it allows almost free slip of the grains. The driving mechanism for the stainless-steel internal cylinder is a stepper with a resolution of 0.36° per step, controlled by a computer and connected to a coaxial mechanical gear (1:6) in order to increase the torque. The gear reduction also increases the resolution of the driving mechanism to 0.06° per step of the internal cylinder. The stepper has a vertical axis, is not fixed, and a counterbalance torque is obtained using an iron beam, instrumented with strain gauges in order to estimate the torque. In principle, measuring the torque allows the mean wall stress to be evaluated. Unfortunately, due to mechanical imperfections in the gear system and the poor dynamic response of the overall system, the signal/noise ratio is too low, especially in the presence of a sand–water mixture, so we did not use the signal of the torque measurement system.

Tests were carried out with a mixture of water and artificial grains used for thermal insulation purposes (commercial name Leca), made of clay. The grains were sorted to have a diameter of $d = 0.25$–0.50 mm. They are almost spherical, and have a specific weight in water nearly equal to 1.0. This low value is due to the presence of air included in the particles during the production process; sorting for the specific weight was necessary to eliminate floating particles. The choice of almost neutrally buoyant particles was forced by the need to reduce to a minimum the normal effective stress increment due to gravity, which would reduce grain mobility, especially in the deeper layers.

The maximum solid fraction (the solid fraction is also defined as the void concentration of the grains, i.e., the ratio between the volume of sediments and the bulk volume) for random packaging was determined by measuring the bulk volume of the grains at rest, the weight of the sample, and the specific weight, obtaining a value of $C_0 = 0.643$. During motion, the solid fraction is reduced due to particle dilatancy and resuspension, achieving a computed mean value of granular void concentration of $C \sim 0.56$.

3.2. Measurements

Measurements were carried out in the Laboratory of Civil Engineering "Paolo Lamberti" of the University of Ferrara, using a commercial TSI particle image velocimeter with a 2048 × 2048 pixel video camera, fitted with a 50 mm/f lens. The light source was a Solo Nd:YAG III dual laser head with maximum repetition rate of 15 Hz and maximum output energy of 50 mJ, water cooled, and mounted on the same side of the video camera. Usually, the laser has a cylindrical lens to generate a light sheet; for the present purposes, the lens was removed and substituted with two cylindrical lenses in series and with mutually orthogonal axis in order to enlarge the beam transforming the laser beam in a light spot able to illuminate the area detected in the frames of the videocamera; polarized lenses were added to the video camera in order to eliminate reflections.

The laser light illuminates frontally the particles moving near the transparent wall of the cell and only occasionally can reach the second layer of particles, with the probability to go further in depth reduced at high grain concentration. Hence most of the signal is scattered by the particles near the wall. The position of the camera and the lens focus were chosen in order to have a depth of field of 20 mm that ensures an acceptable sharpness of the image for all of the frame. We checked the overall performance of the measurement system by gluing a sheet of paper with random dots to a rotating circular plate moved by a stepper motor, exactly in the same configuration of the tests. The measured velocity was within 1% of the expected values.

A similar condition was also met by using LDA in a granular stream [6].

The acquisition frequency of the couple of images was 3.75 Hz, with a time interval between the two images ranging from 600 to 1000 μs depending on the maximum particle velocity and gradient of velocity. In the tested condition, PIV measures the velocity of the grain particles, which in subsequent frames appear much brighter than the small particles always present in the interstitial fluid.

The curvature of the PMMA cylinder and the refraction generate image distortion; an additional distortion is due to the lenses of the video camera. We performed a numerical correction to the acquired data using an algorithm with experimental parameters. The algorithm elaborates the transformation of the pixel position on the CCD of the camera onto a metric position in the plane space equivalent to the rolled cylinder.

The transformation is in terms of quadratic polynomials,

$$\begin{aligned} x_{\text{corr}}/x_{\text{meas}} &= L_x\,(x_{\text{meas}}, y_{\text{meas}}) \equiv a_1 x_{\text{meas}}^2 + b_1 y_{\text{meas}}^2 \\ &\quad + c_1 x_{\text{meas}} + d_1 y_{\text{meas}} + e_1 \\ y_{\text{corr}}/y_{\text{meas}} &= L_y\,(x_{\text{meas}}, y_{\text{meas}}) \equiv a_2 x_{\text{meas}}^2 + b_2 y_{\text{meas}}^2 \\ &\quad + c_2 x_{\text{meas}} + d_2 y_{\text{meas}} + e_2, \end{aligned} \tag{1}$$

used to correct both coordinates. L_x and L_y are the polynomial operator symbols adopted for correcting the two coordinates. The coefficients of the polynomials are estimated using the maximum likelihood criterion. The correction function could also be evaluated using the criteria of geometrical optics, but this is more complicated; there are no real advantages compared to the adopted polynomials.

Calibration requires the following steps. (1) Acquisition with the video camera of a regular grid of 1.0 cm squares, stuck on the external surface of the PMMA cylinder. It is necessary to fix the position of the video camera in order to maintain the same point of view during tests. (2) Estimation of the coordinates (in pixels) of the knots of the grid, using the acquired image. (3) Minimization of the residuals, summed for all knots of the grid and parametric in the coefficient of the interpolating polynomials, allowing the coefficients to be evaluated.

The estimated coefficients have an uncertainty of ∼2% at the 95% confidence level. The maximum correction (near the lateral boundaries) is about 20%. Image elaboration was carried out using an interrogation window of 32 × 32 pixels (∼8 × 8d) with 50% overlap. The result is a matrix of vectors in the knots of a square grid, 16 pixels large, corresponding to 1.25 mm (∼4d).

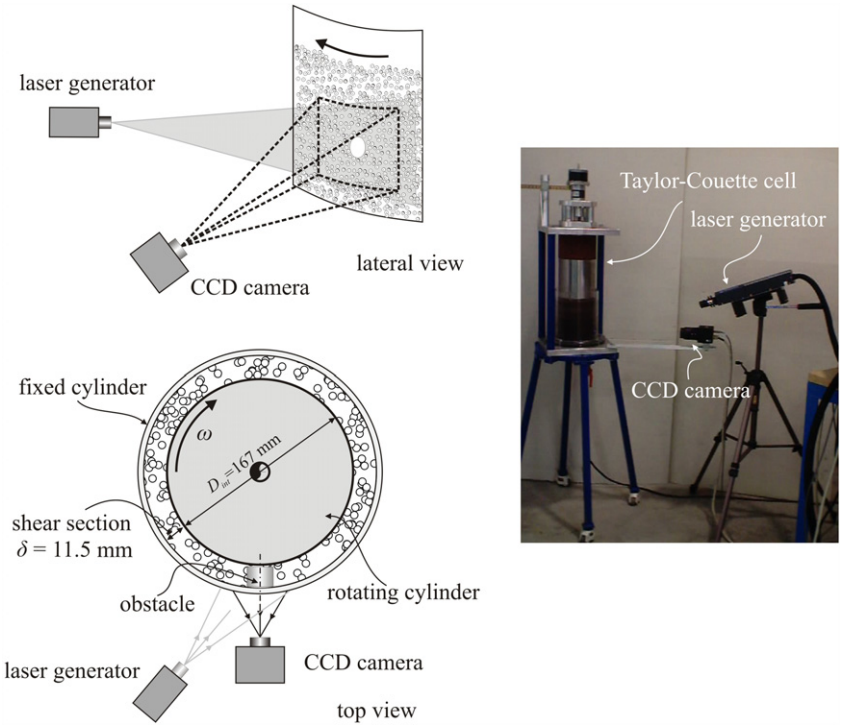

Fig. 1. Schematic diagram of the experimental set-up.

Although the grid, for practical purposes, is stuck on the external surface of the PMMA cylinder (whereas the observed grain particles move near the internal surface), the algorithm does not correct for refraction. This is one of the reasons for the reduced validation rate near the lateral boundaries of the frame, where refraction is more evident. The output files contain the coordinates (in pixels) of the interrogation window and the two components of the space vector at time t (first frame) and $t + \mathrm{d}t$ (subsequent frame). Applying the transformation, a matrix containing the velocity vector in the knots of an irregular grid (the transform of the space vector at time t) is obtained. For easy use and subsequent elaboration, the matrix is interpolated by a regular grid with square length equal to 1.3 mm. For each test, 100 couples of frames were acquired, corresponding to ∼27 s.

3.3. The experiments

In this analyzed series of tests, the obstacle is a circular cylinder with a diameter $D = 15$ mm and a height of 9 mm. The cylinder is glued to the internal surface of the PMMA cylinder and has its axis in the radial direction, ∼50 mm over the bottom of the Taylor–Couette cell. The free surface of water at rest is at ∼150 mm, while the grain bottom is 20 mm below the free surface. A gap of a few millimetres is present between the obstacle and the internal rotating cylinder in order to avoid particle locking. At the maximum rotation rate of the internal cylinder, the mixture looks almost homogeneous, with the mean void concentration of the sediments reduced to 87% of the void concentration of the sediments at rest. The mean void concentration of the sediments during shearing was evaluated by measuring the initial volume of water and of sediments at a value of $C = 0.557$.

The variation in void concentration of the sediments is greater near the free surface in the gap than near the obstacles. Measurements were carried out imposing a rotation rate of 50–200 rpm, corresponding to a lateral velocity of the internal cylinder of 440–1760 mm/s. The undisturbed flow field (without the obstacle) is quite regular, with shear in the radial direction and in the horizontal plane. The theoretical mean value of the shear rate in the radial direction and the mean velocity near the external (transparent) wall are shown in Table 1. The real mean value of the shear rate in the radial direction is less than the theoretical value, due to modest slip of the grains in the presence of the sandpaper.

The shear in the radial direction is not uniform, with higher values near the driving wall. In most of the flow field, the shear rate is much smaller than the average shear rate, and an almost uniform flow is obtained, with minimal effects of curvature of the trajectories due to the annular gap. In fact the minor efficiency in transferring momentum by the driving wall to the granular mixture is due to the increment in the pseudotemperature level near the driving wall: the grain concentration locally reduces and a boundary layer of bouncing sediments develops. It is equivalent to a slip of the grains. At 200 rpm, the measured velocity of the grains near the external cylinder is smaller than that measured at 150 rpm, presumably due to emerging instabilities in the flow field. In order to qualify the flow regime, we introduce the Bagnold number, defined as

$$\mathrm{Ba} = \frac{\rho_s d^2 \lambda^{1/2} \Gamma}{\mu}, \tag{2}$$

where ρ_s is the density of the solid phase, d is the particle diameter, λ the linear concentration of the solid phase, Γ the shear rate, and μ the fluid viscosity. The linear concentration is related to the solid fraction by

$$\lambda = 1/\left[(C_0/C)^{1/3} - 1\right]. \tag{3}$$

For using the mean radial shear rate in Table 1, the Bagnold number is well below the limit for quadratic variations in the stress ($\mathrm{Ba} > 450$) and assumes values in the macroviscous region or at most in the transitional regime. To compute the Reynolds number, defined as

$$\mathrm{Re} = \frac{U_0 D}{\nu_{\mathrm{mixture}}}, \tag{4}$$

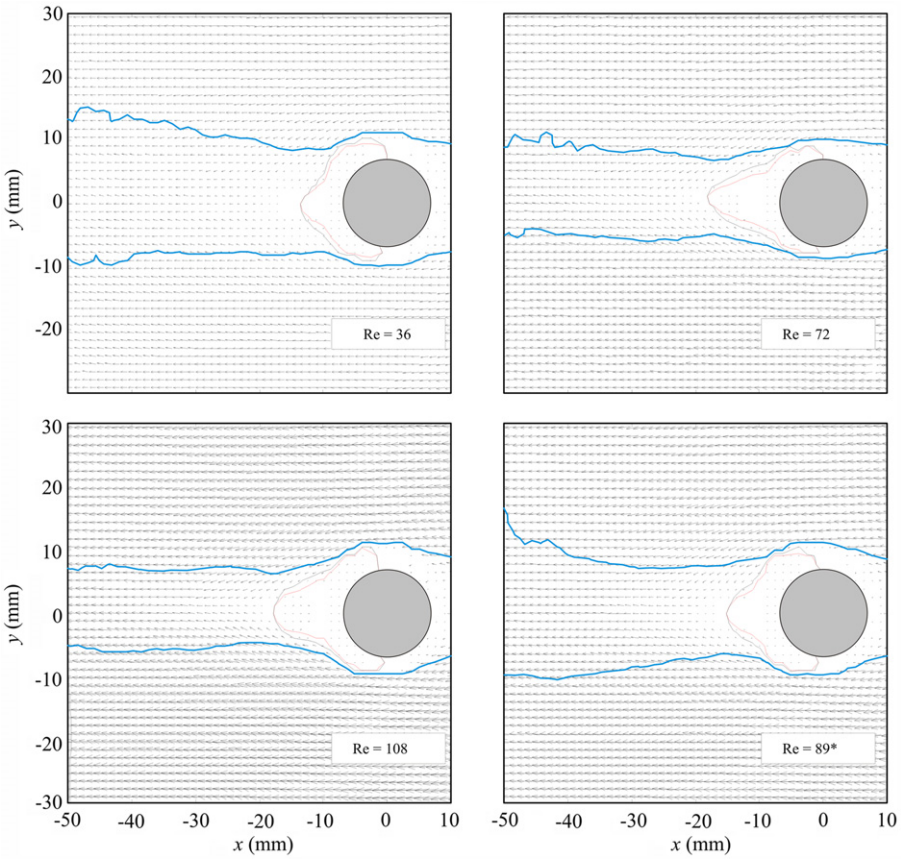

Fig. 2. Average flow field, 100 frames (∼27 s). The curves limit the wake boundary.

Table 1
Imposed velocity scales.

Imposed rotation rate (rpm)	Computed lateral velocity of the driving wall (mm/s)	Measured asymptotic velocity of flow U_0 (at the transparent wall) (mm/s)	Mean radial shear rate (s^{-1})	Bagnold number (.)	Reynolds number (.)
50	440	305	11.7	7.5	36
100	880	615	23.0	15	72
150	1320	920	34.8	22	108
200	1760	760	87.0	56	89

we assume a kinematic viscosity of the mixture equal to

$$\nu_{\text{mixture}} = 2.2\lambda^{3/2}\nu. \quad (5)$$

Near the obstacle, the proper scale of the shear rate is computed by using the asymptotic velocity scale and the thickness of the boundary layer; the linear concentration dramatically increases and the Bagnold number is much greater than 450.

4. Results and discussion

4.1. Flow velocity fields

The presence of the obstacle modifies the flow patterns, with a low-velocity zone upstream, a stagnation or dead zone (sediments at rest) downstream, a boundary layer at the interfaces with the dead zone and the obstacle, a wake, and a recirculating zone at the beginning of the wake. The average flow fields (100 couples of frames, ∼27 s) for all useful tests are reported in Fig. 2, with details shown in Fig. 3. In the upstream region, a domain of grains almost at rest and finally at contact with the body is subject to a strong normal stress transferred by the incoming granular stream. A network of contact forces among grains represents the ultimate mechanism of drag action; the grains almost at rest modify the apparent shape of the obstacle. Stress fluctuations of the incoming stream prevent static stress transfer and continuously change the pattern of the network, with worming movement of the grains. Note that there is no slip condition at the interface with the body (the obstacle is smooth), but here the grain movement is limited anyway by the reduced degree of freedom due to increased grain volume concentration. Occasionally some bulk movement of the grains near the obstacle occurs, due to stick and slip phenomena triggered by disturbances in the incoming granular stream, but the frequency and size of the grain clusters involved are much smaller with respect to dry granular flow [4]. The lubricating effect of water favours small adjustments with worming of the grains, avoiding stress accumulation and hence fast instability of the grain clusters.

Past the obstacles, grains are shed with respect to the incoming granular stream, and are solicited by the action of the weak flow in the recirculating zone. Stress is transferred by a network of contact forces, but the integral action on the body is negligible. Essentially, the particles are at rest because a small pressure guarantees contact with the body and avoids detachment.

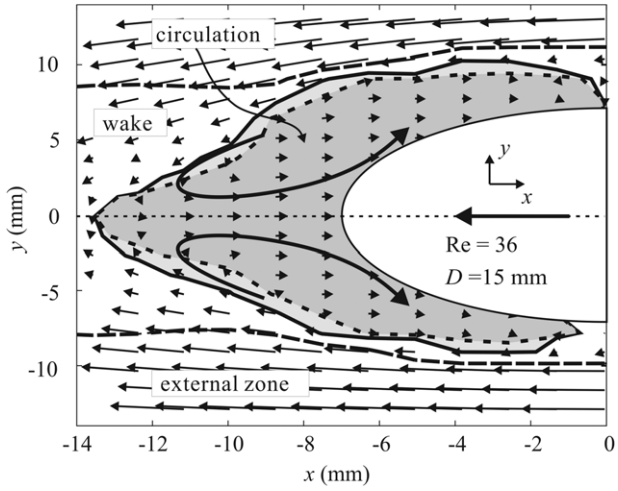

Fig. 3. Mean flow past the circular body. The thick line represents the recirculating zone. The internal dashed line is the locus of zero velocity, and the external dashed line limits the wake boundary. The picture is distorted for easier visualization. Average of 100 frames (∼27 s).

Table 2
Length of the recirculating zone.

Asymptotic velocity U_0 (mm/s)	Reynolds number (.)	Length of the recirculating zone (measured from the boundary of the cylinder body) x (mm)
305 (50 rpm)	36	6 ($L/D = 0.24$)
615 (100 rpm)	72	10.7 ($L/D = 0.43$)
920 (150 rpm)	108	10.3 ($L/D = 0.41$)
760 (200 rpm)	89	7.6 ($L/D = 0.30$)

This behaviour is different than that observed for dry granular flows. For a cylinder in a dry granular flow stream [14,4], downstream of the cylinder an empty region occurs, the consequence of a limited granular temperature that cannot overcome the particle inertia and hence cannot push the grains in the transverse direction. In addition, cohesionless grains cannot sustain the tensile loads that develop at the trailing edge of the cylinder.

In the wake, there is a deficit of momentum that favours the transfer of momentum from the external zone. In addition, there is drag action of the internal cylinder. The defect velocity tends to decrease downstream, but unfortunately the extent of the wake cannot be measured properly in the apparatus used for tests.

The recirculating zone is due to the merging of separated shear layers that form a steady symmetric closed near-wake. In the recirculating zone (thick line in Fig. 3, computed imposing a zero net volume flux), there are two counter-rotating vortices, while the average velocity is a few mm/s. Note that the most correct computation of the recirculating zone should be based on mass flux and hence the grain void concentration should be known. In all tests, the maximum extent downstream measured from the boundary of the cylinder (Table 2) is a small fraction of the diameter of the obstacle, except for the maximum rotation rate test (200 rpm), presumably characterized by instabilities of the flow. The shape of the recirculating zone is almost independent of the asymptotic velocity, but its maximum extent tends first to increase, and then to decrease at higher asymptotic velocities.

On observing the range of the Reynolds number and comparing it with similar results obtained for cylinders invested by a single-phase Newtonian fluid, we conclude that the regime is viscous even at the highest incoming asymptotic velocity. The length variation of the recirculating zone has a similar trend, but is an order of magnitude smaller. For the granular mixture (present experiments), for Re < 72, we get

$$L/D = 0.006\mathrm{Re}, \tag{6}$$

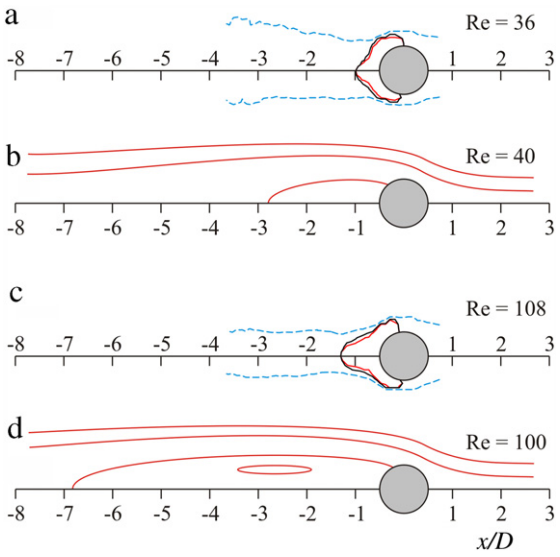

Fig. 4. Comparison between the flow field measured in the present experiments (panels (a) and (c)) and computed for a Newtonian fluid by Fornberg [15] (panels (b) and (d)).

while for homogeneous Newtonian fluids in the range $4.4 < \mathrm{Re} < 40$ [8], we get

$$L/D = 0.05\mathrm{Re}. \tag{7}$$

A comparison between the experimental results of the present study and the numerical integration results for Newtonian fluids [15] is shown in Fig. 4. The geometry of the recirculation zone is very different, especially for increasing Reynolds number. Note that the results of Fornberg numerical integration give a larger extension of the recirculation zone with respect to that indicated in Eq. (7).

4.2. Granular temperature and principal axes of the kinetic stress tensor

In Fig. 5, the mean variance of the grain velocity (defined as 'granular temperature', even though a proportional coefficient is missing in the expression), expressed as

$$T = \overline{\left(U_x - \bar{U}_x\right)^2} + \overline{\left(U_y - \bar{U}_y\right)^2} \equiv \overline{U_x'^2} + \overline{U_y'^2}, \tag{8}$$

is shown for the test with Re $= 36$. The overbar indicates time average. The fluctuation is computed with respect to the local mean for each spatial point.

The granular temperature is the trace of the kinetic stress tensor (equivalent to the Reynolds stress tensor); it represents a measure of the grain fluctuations, and, when the transport terms are negligible, it is usually larger in the source areas. The source is essentially due to the shear rate, and the granular temperature in local equilibrium is proportional to the square of the shear rate. In the present tests, the minimum granular temperature is reached in the dead zones upstream and downstream, near the boundaries of the obstacle, where friction is dominant. The hot zones define the wake; they are due to the high shear rate and they help the momentum flux from the external zone to the wake, progressively reducing the defect velocity. The granular temperature distribution is quite similar for all tests and shows a little asymmetry, with smaller values near the bottom of the cell. The asymmetry is due to the increasing grain volume concentration toward the bottom of the cell, because of the combined (limited) effects of gravity and the boundary effects imposed by the rigid wall; in fact, at higher grain void concentrations, collisional and frictional stresses are

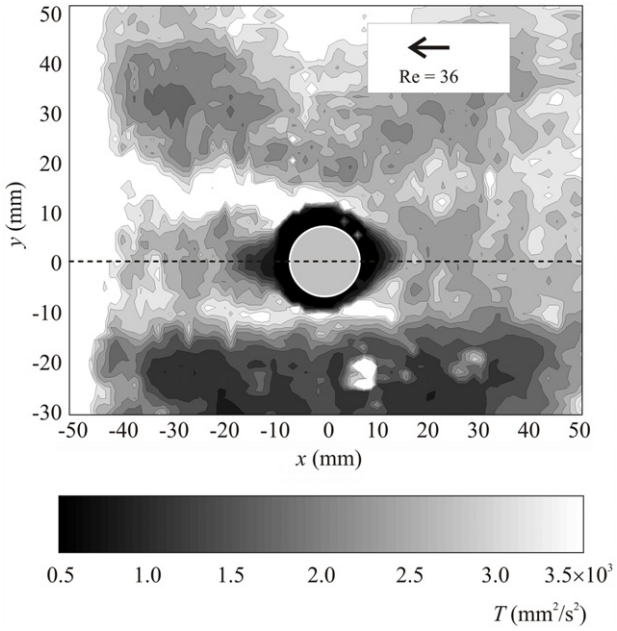

Fig. 5. Mean granular temperature. The 'cold' zones are dark.

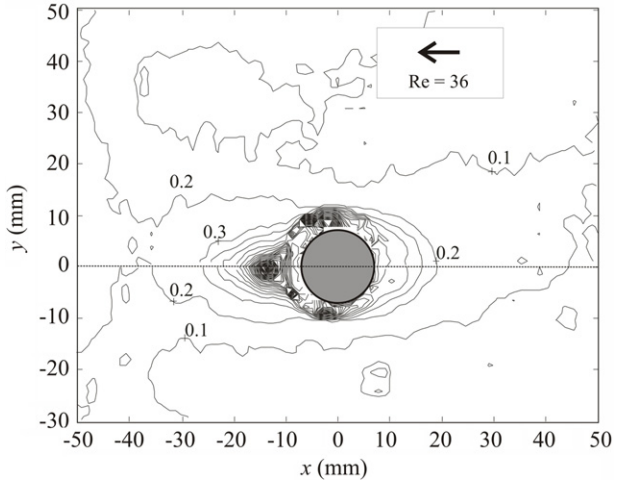

Fig. 6. Index of turbulence. Average value on 100 frames (∼27 s).

dominant. The observed granular temperature distribution is quite different from that observed in a dense dry granular flow around an immersed cylinder [4]. In that case, hot spots occur past the obstacle where a free surface exists.

The average turbulence index, defined as

$$\gamma = \left(\frac{\overline{U_x'^2} + \overline{U_y'^2}}{\bar{U}_x^2 + \bar{U}_y^2} \right)^{1/2}, \tag{9}$$

is shown in Fig. 6. The maxima are in the dead zone, where the average velocity is almost zero, and fluctuations due to grains in motion and stick–slip phenomena dominate. Stick and slip phenomena are regularly observed in dry granular streams but are also present if a lubricant is present.

Note that the data rate of the frames, 3.75 Hz, and the spatial resolution of 8d filter most of the high-frequency fluctuations related to micromechanic collisions, even though the presence of water as an interparticle fluid favours dampening of these fluctuations.

If the temperature is isotropic and the cross-correlation terms are non-zero, the velocity covariance tensor approximates the

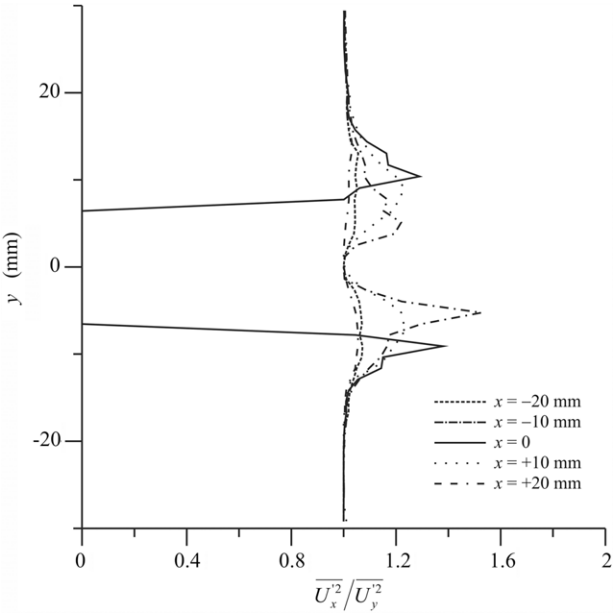

Fig. 7. Measured anisotropy of the granular temperature. Re = 36.

kinetic stress tensor and is collinear with the rate of deformation tensor. There are several reasons for a departure from these conditions: anisotropy of the granular temperature and shear rate effects can significantly modify the orientation of the axes. Some computer simulations reveal the presence of anisotropy in the temperature and normal stresses, especially for low granular void concentrations and dissipative particles in a dry granular stream. According to Campbell [16], the anisotropy should be present only at low solid fractions, where the kinetic transport of particles, without collisions, generates a fluctuating velocity perpendicular to the velocity gradient. In contrast to Campbell's interpretation, some experiments [17] report that the granular temperature is also higher in the stream direction for collisional granular flows down an inclined plane, independent of the value of the solid fraction and of the rough bed nature. No explanation is given by the authors. In general, the effects of pseudotemperature anisotropy are less evident at high granular void concentrations and high elastic restitution coefficient of the grains, and are essentially negligible beyond a critical value of void concentration. The kinetic component of the stress is only a minor fraction of the total stress at high void concentrations of sediments computed for the present mixture. Collisional stress, often with multiple collisions, and frictional stress dominate, and hence only marginal information on the stress tensor can be obtained by analyzing the velocity covariance tensor.

The void concentrations of the grains in the present experiments are relatively high, but the level of dissipation is also high due the presence of water as the interparticle fluid, and hence anisotropy in both normal stresses and temperature should be less evident. Nevertheless, a significant anisotropy of the granular temperature at Re = 36 is evident in Fig. 7. At higher Reynolds numbers, anisotropy is even more evident. As a consequence, a strong rotation of the axes of the tensor is expected.

In order to check the degree of anisotropy, we compared the orientation of the principal axes of the two tensors. A similar analysis was conducted in a dry granular stream with a free surface in a rotating drum [6], concluding that free surface perturbations were responsible for streaming but could justify only part of the non-collinearity of the axes.

The principal axes of the rate of deformation tensor are oriented as

$$\phi_D = \frac{1}{2} \tan^{-1} \left(\frac{U_{x,y} + U_{y,x}}{U_{x,x} - U_{y,y}} \right) \tag{10}$$

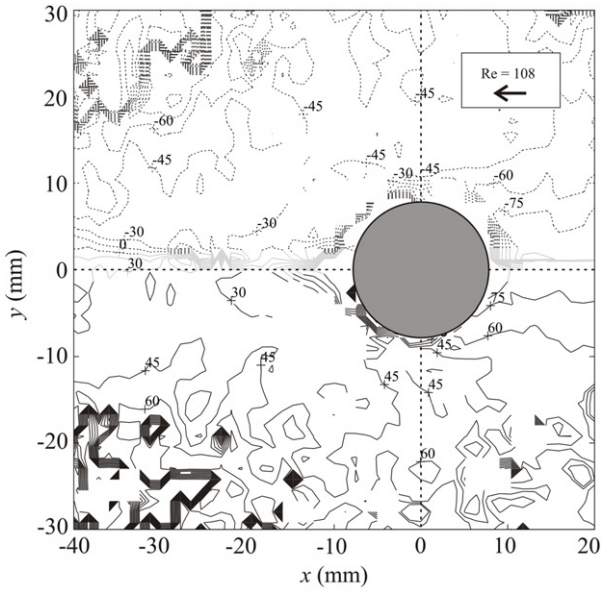

Fig. 8. Angle of rotation between the velocity covariance tensor and the rate of deformation tensor.

(the comma indicates the partial derivative), while the principal axes of the velocity covariance tensor are oriented as

$$\phi = \frac{1}{2}\tan^{-1}\left(\frac{2\overline{U_x' U_y'}}{\overline{U_x'^2} - \overline{U_y'^2}}\right). \tag{11}$$

In Fig. 8, a map of the axis rotations (differences between the nearest principal axes of the two tensors) is shown for one of the tests (Re = 108). The axis rotation is negligible along the symmetry line, and increases upstream and in the wake. The behaviour is almost similar for all tests; such a rotation can be related to the strong streaming in the region past the body and possibly to a non-isotropic dependence of the kinetic stress on the pseudotemperature. In Fig. 9, the principal axes of the velocity covariance and the rate of deformation tensor for Re = 108 at the section $x = 0$ are shown. At least near the cylinder, the axes of the rate of deformation tensor are almost 45° with respect to velocity orientation, as expected in a pure shear rate, and the axes of the velocity covariance are oriented similar to velocity, with a rotation of 45° instead of 0°. This rotation is almost equal to that observed in a dry granular stream [6]. Similar behaviour is observed in the other tests and in different sections.

A normal stress difference has also been derived for homogeneous granular temperature and grain void concentration as a consequence of the Burnett order correction of a Chapman–Enskog-like expansion of the Boltzmann equation [18]. For slightly anelastic particles at a simple low shear rate, the components of the kinetic stress tensors are

$$\begin{aligned}
\sigma_{kx} &\propto T + a\left(U_{x,y}\right)^2 l^2 \\
\sigma_{ky} &\propto T - a\left(U_{x,y}\right)^2 l^2 \\
\tau_{kxy} = \tau_{kyx} &\propto b\left(U_{x,y}\right)\sqrt{T} l,
\end{aligned} \tag{12}$$

where l is the mean free path of the particles and $a = 0.3395$ and $b = -0.4073$ are two coefficients. The ratio between the normal stresses is equal to

$$\frac{\sigma_{kx}}{\sigma_{ky}} \approx \frac{T + 0.679\left(U_{x,y}\right)^2 l^2}{T - 0.679\left(U_{x,y}\right)^2 l^2}, \tag{13}$$

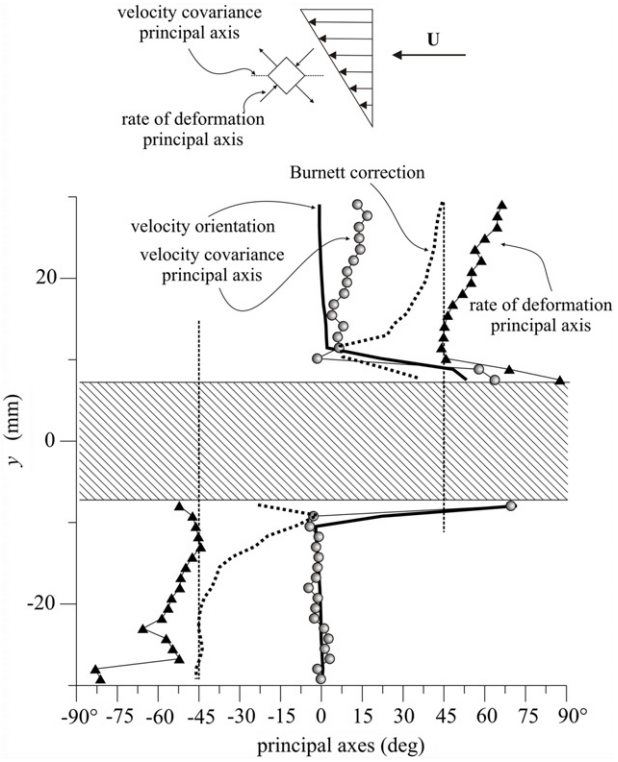

Fig. 9. Principal axes of the velocity covariance and the rate of deformation tensor for Re = 108, section at $x = 0$.

and the principal axes of the kinetic stress tensors are oriented as

$$\phi_B = \frac{1}{2}\tan^{-1}\left(\frac{b\sqrt{T}}{aU_{x,y}l}\right). \tag{14}$$

Note that, in this model, the stress anisotropy is a consequence of the shear and not of the inelasticity. The computed axis rotation induced by the Burnett order correction term is shown as a dotted line in Fig. 9, with the mean free path computed as inversely proportional to the linear concentration. Unless an exaggerated mean free path is assumed, the shear rate is responsible for a minor part of kinetic stress anisotropy and is active only in the zone where the shear effects overcome the granular temperature effects, near the body. Note that the Burnett order correction is strictly valid only if the elasticity of the particles is high, which is not the case for particles with a liquid as the interparticle fluid.

4.3. Length scales

The correlation functions can provide additional information on the structure of turbulence through the macroscale and the microscale. The macroscale Λ_{ij_k}, corresponding to the cross-correlation between the velocity components i and j in direction x_k, is generally defined in isotropic homogeneous conditions as

$$\Lambda_{ij\_k} = \int_0^\infty R_{ij}\left(\Delta x_k\right) dx_k. \tag{15}$$

In the flow field of the present tests, both inhomogeneity and anisotropy occur, and considering the dataset of measurements, a better definition of the integral macroscale is

$$\Lambda_{ij\_k}\left(x_k\right) = \frac{1}{2}\int_{-\infty}^{\infty} R_{ij}\left(x_k, x_k'\right) dx_k'; \tag{16}$$

i.e., the integral macroscale refers to cross-correlation in the direction x_k of the two available velocity components, and is

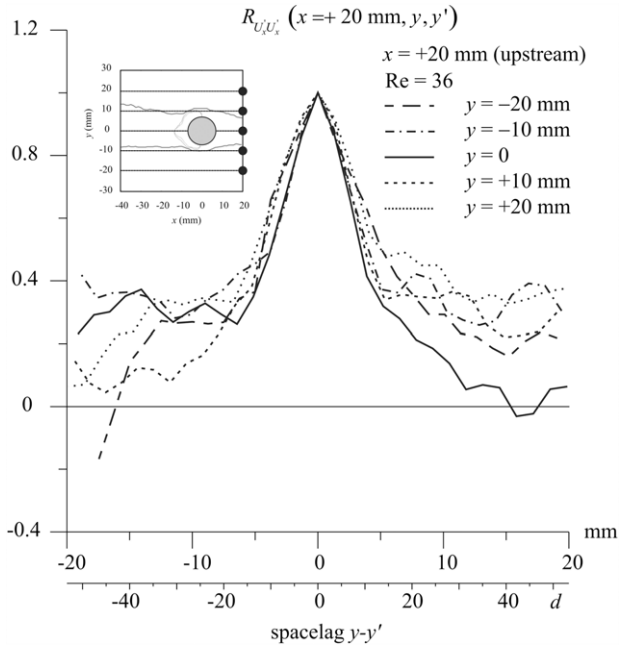

Fig. 10. Autocorrelation function $R_{U'_xU'_x}(x=+20\text{ mm}, y, y')$ of the streamwise velocity component in the spanwise direction (y) for several points at $x=+20$ mm (upstream) Re = 36.

also a function of position. The case $i = j$ is straightforward, and is computed using the autocorrelation. The computed autocorrelation functions at $x = 20$ mm (upstream) and at several points are shown in Fig. 10.

The integral macroscales represent a characteristic size of the large eddies advecting the mixture in the corresponding direction of evaluation. In Fig. 11, the integral macroscales are reported in the wake ($y = 0$ and $y = +10$ mm) and near the boundary with the external zone ($y = 20 +$ mm). In the middle of the wake, the eddies are almost symmetric, with $\Lambda_{xx\_x} \sim \Lambda_{xx\_y}$, and with a size $\sim 1/3$ of the transverse size of the wake, slowly increasing from $\sim 10d$ to $\sim 20d$ 40 mm downstream (scales computed using the streamwise velocity autocorrelation). Moving towards the boundary of the wake, the macroscales increase to $\sim 50d$ (almost equal to the transverse size of the wake), and the streamwise correlation Λ_{xx_x} becomes dominant with respect to the spanwise correlation (Λ_{xx_y}); i.e., the vortices have an elliptical section with maximum axis along the main stream direction. When observing the integral macroscales Λ_{yy_y} computed using the autocorrelation of the spanwise velocity components, a series of stationary periodic vortices in the external region and near the boundary of the wake is discovered (Fig. 12). In fact, the scales computed at $y = +20$ mm show a periodicity of ~ 10 mm ($\sim 26d$) in the streamwise direction, progressively damped downstream. Such periodicity is also present in the wake, but is not detected for higher Reynolds number tests.

The Taylor microscale is frequently used, defined as

$$\lambda^2_{ij\_k} = -2\left|\frac{\partial^2 R_{ij\_k}}{\partial x_k^2}\right|_{x_k=0}. \tag{17}$$

This is not the smallest scale, but is often assumed as the length scale where most dissipation takes place.

With the goal of finding the relation between the macroscale and the microscale, we checked the dependence of the Taylor microscale on the Reynolds number, expressed as

$$\mathrm{Re}_\Lambda = \frac{\Lambda U}{\nu}, \tag{18}$$

with U the local velocity scale. Assuming a local balance in isotropic turbulence [19], production equals dissipation, and the relation between the microscale and the macroscale is

$$\frac{\lambda}{\Lambda} \propto \mathrm{Re}_\Lambda^{-1/2}. \tag{19}$$

If the local energy balance is not satisfied, still adopting the hypothesis of small-scale isotropy at large Reynolds numbers, a possible expression of this dependence is

$$\frac{\lambda}{\Lambda} \propto \mathrm{Re}_\Lambda^{n}. \tag{20}$$

While along the axis of symmetry the Reynolds number is very low and no evident correlation can be drawn, in the external region near the boundary of the wake ($y = +20$ mm) the

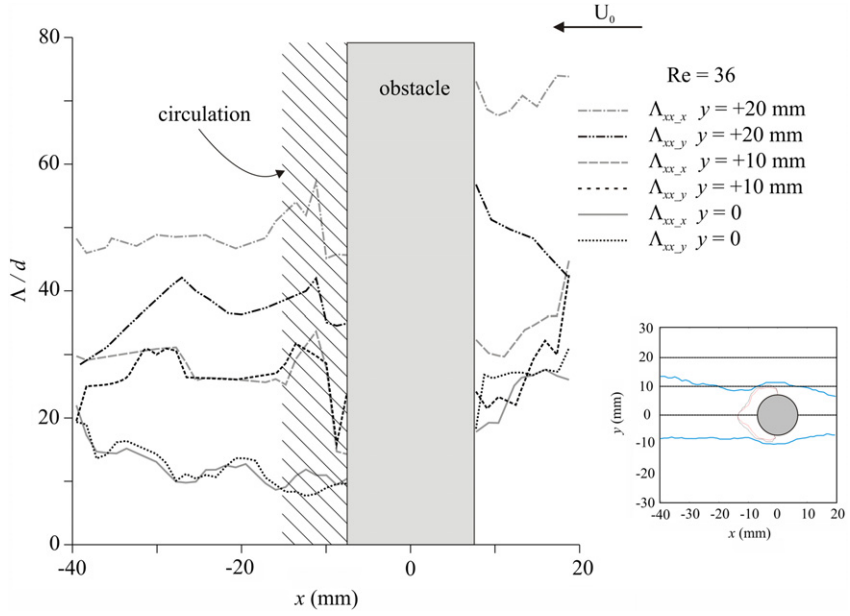

Fig. 11. Macroscale in the streamwise direction (x) and in the spanwise direction (y) of the streamwise velocity component (U'_x) at $y = 0$ (axis of symmetry of the wake), $y = 10$ mm and $y = 20$ mm. Re = 36.

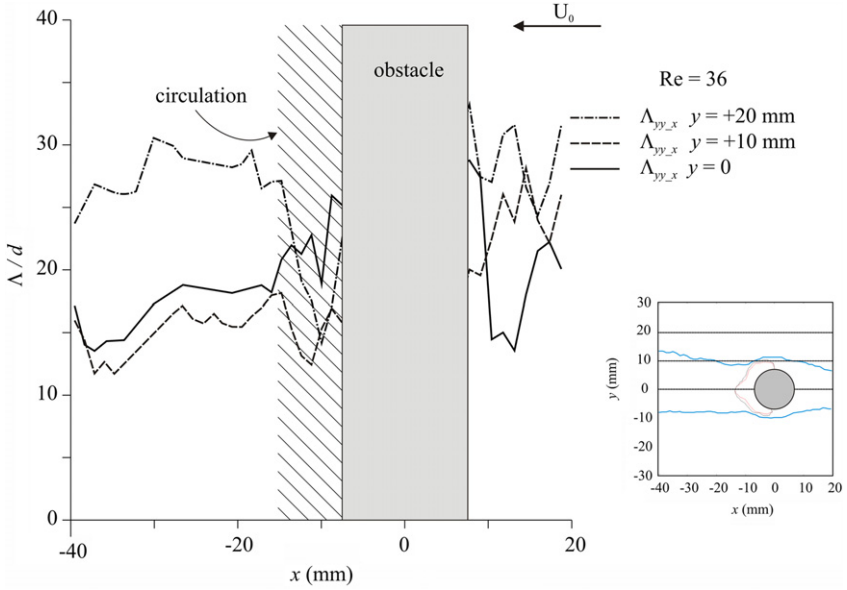

Fig. 12. Macroscale in the streamwise direction (x) of the spanwise velocity component (U_y') at $y = 0$ (axis of symmetry of the wake), $y = 10$ mm and $y = 20$ mm. Re = 36.

Taylor microscale (its ratio with the macroscale) decreases with the Reynolds number more quickly than it generally does in the case of local energy balance, with $n = -0.85$ at 100 rpm and $n = -0.6$ at 150 rpm. Considering that the Taylor microscale is adopted as the scale of dissipation, reducing its value to balance energy production at a faster rate than the local equilibrium hypothesis means that there is a large influx of energy due to transfer from other regions of the flow field.

4.4. The wake past the obstacle

Downstream of the obstacle there is the wake, with a mean velocity lower than the external velocity and an almost symmetric velocity profile similar to the velocity profile in the wake of a Newtonian fluid.

In Figs. 2 and 4, the wake is represented as limited by velocity equal to 50% of the axial defect velocity $U_s(x)$ (with respect to the asymptotic velocity, i.e., the velocity in the external region in the same section). This definition differs slightly from the classical defect velocity definition, which refers to the undisturbed velocity. The local width of the wake l is often assumed as the geometric transverse scale, whereas the defect velocity is assumed as the transverse velocity scale.

For turbulent wakes of Newtonian fluids in a two-dimensional flow field at high Reynolds numbers, the velocity profile becomes self-similar at a distance $>80\,D$, with $l \propto x^{1/2}$ and $U_s \propto x^{-1/2}$ [19].

The spatial characteristics of the wake for the present tests are shown in Fig. 13. For the test at Re $= 36$, the velocity scale has a logarithmic decay, according to the following expression:

$$\frac{U_s}{U_0} = \ln\left[\alpha\left(\frac{x' - D/2}{D}\right)^{\beta}\right]$$
$$D < x' < 4D \text{ with } \alpha = 1.57 \pm 0.8\%;$$
$$\beta = -0.33 \pm 3.2\%. \tag{21}$$

The parameters were computed using the least-squares method, with $R^2 = 0.989$ at a confidence level of 95%.

In all other tests, the velocity scale decays linearly, according to the following expression:

$$\frac{U_s}{U_0} = a - b\left(\frac{x' - D/2}{D}\right) \quad \text{for } D < x' < 4D. \tag{22}$$

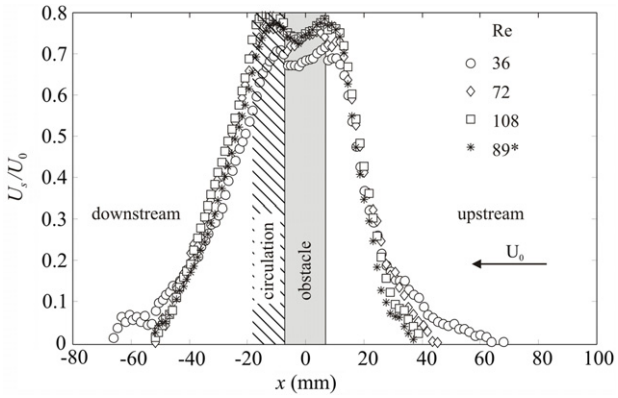

Fig. 13. Upstream and downstream variation of the velocity scale U_s. All tests.

Table 3
Parameters of the function in Eq. (22). The uncertainty is at the 95% confidence level.

Test (rpm)	Re	a (%)	b (%)	R^2
100	72	0.88 ± 1.4	0.31 ± 4.3	0.988
150	108	0.93 ± 2.8	0.33 ± 4.2	0.987
200	89	0.81 ± 4.7	0.29 ± 6.4	0.972

The values of estimated parameters are shown in Table 3.

Fig. 14 shows the spatial evolution downstream and upstream of the transversal length scale.

The data are less coherent than for the velocity scale. For the tests with Re $= 72$ and Re $= 108$, the length scale is almost constant or slightly increasing downstream.

The interpolating functions have the following expression:

$$\frac{l}{D} = c\left(\frac{x' - D/2}{D}\right)^{n}, \quad D < x' < 3D, \tag{23}$$

with the parameters estimated by the least-squares method shown in Table 4.

In principle, the behaviour of the wake for the granular stream generated in the present apparatus should be similar to the behaviour of a homogeneous Newtonian fluid, because the regime is macroviscous. In practice, the observed discrepancies can be attributed to the limited extent of the flow field, which can favour

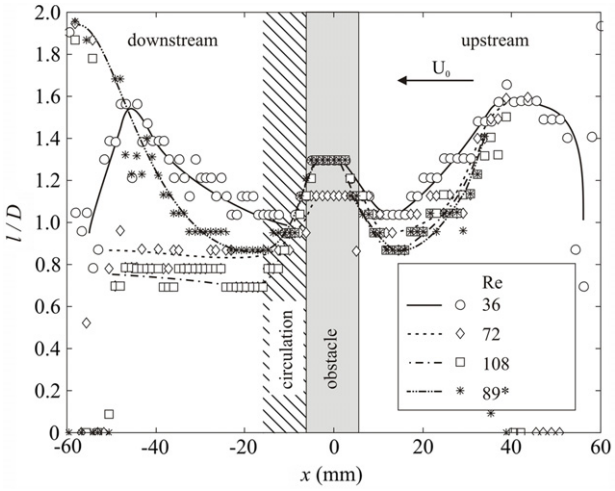

Fig. 14. Upstream and downstream transversal length scale. All tests.

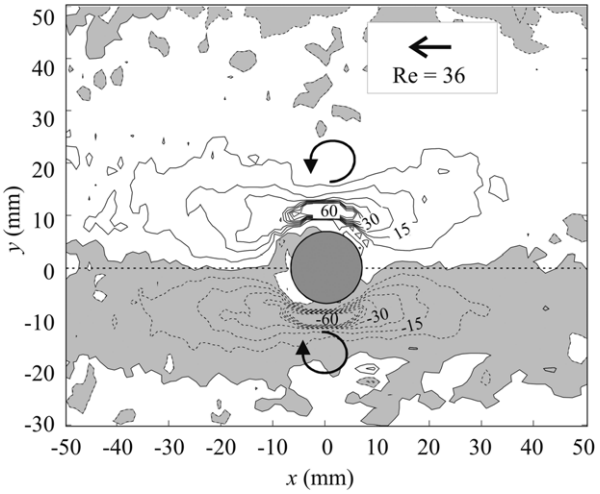

Fig. 15. Mean vorticity; the values are in s^{-1}. Re = 36.

Table 4
Parameters of the interpolating function in Eq. (23). The uncertainty refers to a 95% confidence level.

Test (rpm)	Re	c (%)	n (%)	R^2
50	36	1.13 ± 4.6	0.22 ± 27	0.67
100	72	0.76 ± 4.0	0.1 ± 65	0.26
150	108	0.72 ± 2.7	0.06 ± 73	0.23
200	89	0.91 ± 5.1	0.37 ± 22	0.75

effects of the wake on the incoming stream at high rotation rates; no observation can be confidently made at a distance where self-similarity occurs. The expected (modest) grain void concentration variability is a second source of discrepancies.

4.5. Vorticity and divergence

The flow field is essentially two dimensional, and only the radial component of the vorticity is present. The average vorticity is shown in Fig. 15. Two macrovortices are evident near the upper and lower separation points, and two smaller macrovortices appear in the recirculating zone. Near the bottom and the free surfaces, there are some footprints of locally generated vorticity. To compare the vorticities of different tests, the non-dimensional vorticity

$$\widetilde{\omega_z} = \frac{\omega_z D}{U_0} \tag{24}$$

is reported in the vertical at $x = 0$ (Fig. 16). Except for the lowest rotation rate, the profile is similar for all tests. Vorticity is confined within $\pm 0.75D$; the maximum non-dimensional intensity is ± 4. The variance of vorticity (not shown) is almost uniform, with small values in the whole domain. This means that, at least in the analyzed conditions, no von Karman vortices develop, even though the frequency of acquisition can be a limiting factor. The frequency of shedding of the vortices is usually expressed in terms of the Strohual number and of the Reynolds number. According to Rayleigh [20], an empirical formula exists:

$$\mathrm{St} = 0.195\left(1 - \frac{20.1}{\mathrm{Re}}\right), \qquad \mathrm{St} = \frac{fD}{U_0}, \tag{25}$$

where f is the frequency of shedding. Rayleigh's expression is plotted in Fig. 17 with some experimental data [21]. The expected frequencies of shedding for the present tests are all much larger than half the frequency of acquisition of the particle image velocimeter (Nyquist's theorem requires a frequency of acquisition at least twice the maximum expected frequency in the signal),

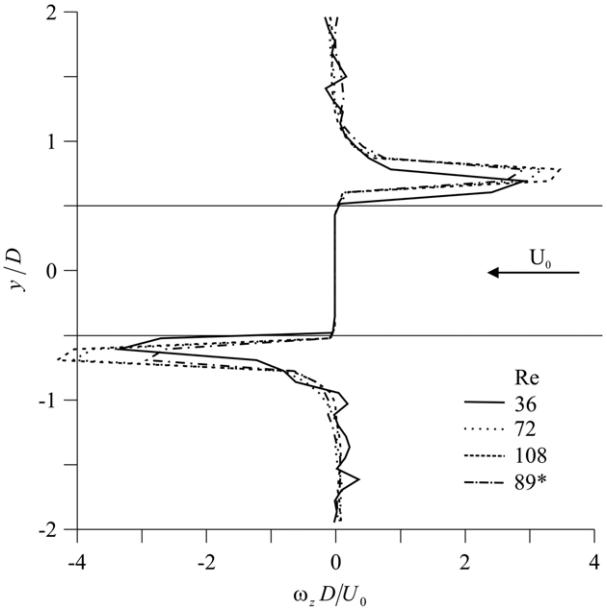

Fig. 16. Non-dimensional vorticity at $x = 0$. All tests.

except probably for the lowest Reynolds number, which is below the minimum experimental range that has revealed the shedding of the vortices.

Fig. 18 shows a typical divergence field. In stationary conditions, the mass conservation equation for the granular phase can be written as

$$\mathbf{U} \cdot \mathrm{grad}(\ln \rho) = -\mathrm{div}\ \mathbf{U}, \tag{26}$$

where ρ is the bulk density of the grains. Along the symmetry axis, the spanwise velocity U_y is almost negligible with respect to the streamwise velocity (it should be rigorously zero), and Eq. (26) can be integrated to obtain the grain volume concentration:

$$\frac{\rho}{\rho_0} \equiv \frac{C}{C_0} = \exp\left(\int_{x_0}^{x} \frac{-\mathrm{div}\ \mathbf{U}}{U_x} dx\right), \tag{27}$$

where ρ_0 is the bulk density of the grains in section x_0 and C and C_0 are the corresponding volume concentrations of the grains. The results of the integration, carried out separately for the downstream and upstream areas, are shown in Fig. 19. The uncertainties are high if the velocity is low, i.e., in the zones near the dead zones. Upstream, the grain void concentration

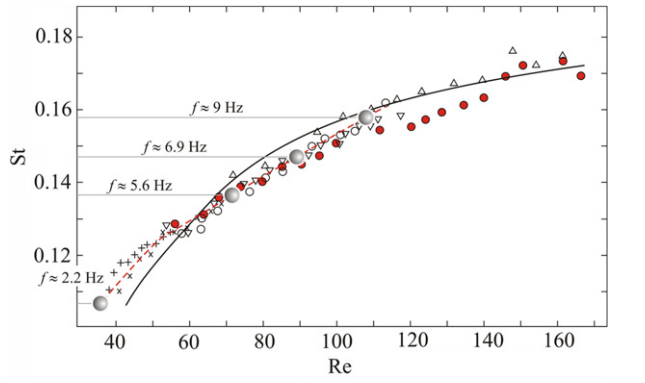

Fig. 17. Variation of the Strohual number in terms of the Reynolds number. ●: present tests. The dashed curve is an interpolation of the experimental data in [21]; the bold curve is Rayleigh's empirical equation (Eq. (25)).
Source: Adapted from [21].

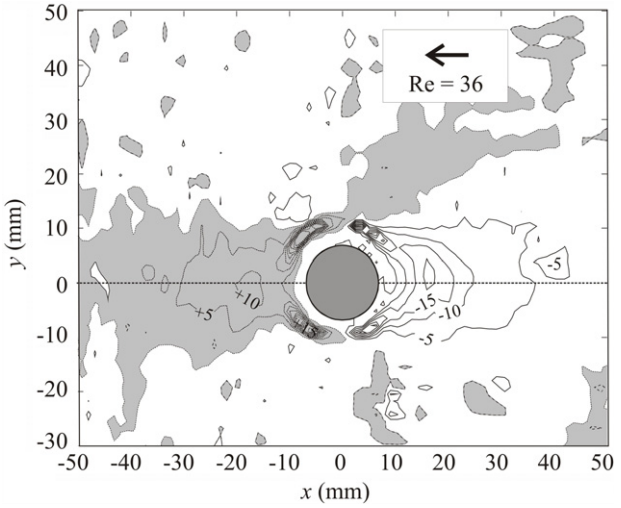

Fig. 18. Mean divergence; the values are in s^{-1}. Dark zones represent positive divergence. Re = 36.

first decreases then increases again, whereas in the wake it decreases monotonically downstream. The results represent only an estimate, because three-dimensional effects play an important role, especially in these zones. The indicative limit value of bulk density is shown by the dashed line, but it is affected by a high degree of uncertainty, considering that even a small increment in bulk density implies an almost immediate halt of the grains.

5. Conclusions

We have obtained grain velocity measurements in a two-dimensional stream of a granular mixture (with water as the interparticle fluid) around a cylinder. The flow field is similar to that of a Newtonian fluid. Flow visualization shows a recirculation zone past the obstacle, a wake zone, and an external zone.

- In the range of the present measurements, with limited Reynolds numbers, no von Karman vortices develop, though the limited frequency of acquisition (3.75 Hz) may be not appropriate to detect them.
- The length of the recirculating zone decreases with the Reynolds number, as for homogeneous Newtonian flows, even though it is an order of magnitude smaller.
- Due to temperature anisotropy and large shear, the kinetic stress tensor and the rate of deformation tensor are not collinear but are 45° rotated. This value is almost equal to that observed in a dry granular stream [6]. The rotation can be partly attributed to shear, on the basis that a Burnett order term correction can also explain the normal kinetic stress difference.
- The integral length scales in the wake slowly increase downstream with respect to the cylinder, suggesting the existence of symmetric macrovortices ∼1/3 the size of the transverse wake. Moving towards the external region, the vortices become elongated in the streamwise direction, with a maximum axis of the order of the wake transverse size. At low Reynolds number, periodic vortices are also detected, with a periodicity in the streamwise direction of ∼36*d*. Checking the balance between the microscale and the macroscale, an energy flux is detected, as expected, from the external region toward the wake.
- The velocity scale of the wake decays linearly downstream (except for low mean velocities of the stream), and the transverse length scale weakly increases. Self-similarity, if any, should be achieved far from the obstacle and is not measurable in the present experiments.
- The vorticity scales with the diameter of the obstacle and with the asymptotic velocity. Vorticity is confined within ±0.75 *D* and reaches a maximum intensity equal to $\sim 4U_0/D$.

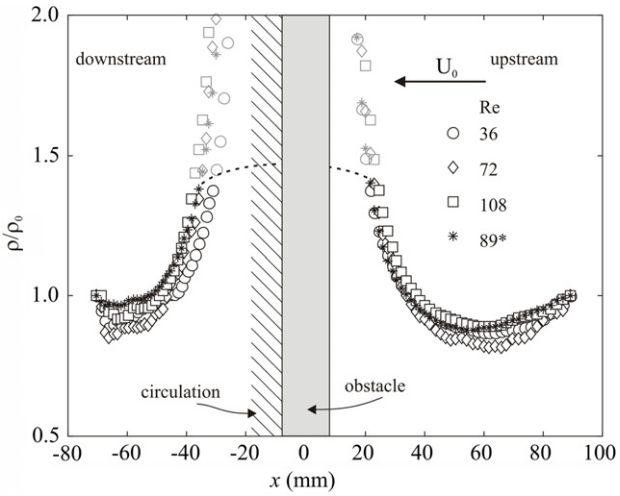

Fig. 19. Bulk density variation along the axis of symmetry. All tests.

References

[1] K. Wieghardt, Experiments in granular flow, Annu. Rev. Fluid Mech. 7 (1975) 89–114.
[2] V. Buchholtz, T. Pöschel, Interaction of a granular stream with an obstacle, Granular Matter 1 (1998) 33–41.
[3] C.R. Wassgren, J.A. Cordova, R. Zenit, A. Karion, Dilute granular flow around an immersed cylinder, Phys. Fluids 15 (11) (2003) 3318–3330.
[4] D. Chehata, R. Zenit, C.R. Wassgren, Dense granular flow around an immersed cylinder, Phys. Fluids 15 (6) (2003) 1622–1631.
[5] J.M.N.T. Gray, Y.-C. Tai, S. Noelle, Shock waves, dead zones and particle-free regions in rapid granular free-surface flows, J. Fluid Mech. 491 (2003) 161–181.
[6] S. Longo, A. Lamberti, Granular shear flow mechanics, Exp. Fluids 32 (3) (2002) 313–325. http://dx.doi.org/10.1007/s003480100359.
[7] R. Deng, C.-H. Wang, Particle image velocimetry study on the pattern formation in a vertically vibrated granular bed, Phys. Fluids 15 (2003) 3718–3729.
[8] M.M. Zdravkovich, Flow Around Circular Cylinders, Vol. 1: Fundamentals, Oxford University Press, Oxford, UK EU, ISBN: 0 19 856396 5, 1997, p. 672+xviii.
[9] T. Sarpkaya, P.G. Rainey, R.E. Kell, Flow of dilute polymer solutions about circular cylinders, J. Fluid Mech. 57 (1973) 177–208.
[10] R.M. Nedderman, S.T. Davies, D.J. Horton, The flow of granular materials round obstacles, Powder Technol. 25 (1980) 215–223.
[11] G. Pilate, M.J. Crochet, Plane flow of a second-order fluid past submerged boundaries, J. Non-Newton. Fluid Mech. 2 (1977) 323–341.

[12] R.A. Bagnold, Experiments on a gravity free dispersion of large solid spheres in a Newtonian fluid under shear, Proc. R. Soc. Lond. Ser. A 225 (1954) 49–63.
[13] M.L. Hunt, R. Zenit, C.S. Campbell, C.E. Brennen, Revisiting the 1954 suspension experiments of R. A. Bagnold, J. Fluid Mech. 452 (2002) 1–24.
[14] J.-C. Tsai, W. Losert, G.A. Voth, J.P. Gollup, Two-dimensional granular Poiseuille flow on an incline: multiple dynamical regimes, Phys. Rev. E 65 (2002) 011306.
[15] B. Fornberg, A numerical study of steady viscous flow past a circular cylinder, J. Fluid Mech. 98 (04) (1980) 819–855.
[16] C.S. Campbell, The stress tensor for simple shear flows of a granular material, J. Fluid Mech. 203 (1989) 449–473.
[17] E. Azanza, F. Chevoir, P. Moucheront, Experimental study of collisional granular flows down an inclined plane, J. Fluid Mech. 400 (1999) 199–227.
[18] I. Goldhirsch, N. Sela, Origin of normal stress differences in rapid granular flows, Phys. Rev. E 54 (4) (1996) 4458–4461.
[19] H. Tennekes, J.L. Lumley, A First Course in Turbulence, The MIT Press, Cambridge, UK EU, ISBN: 0 262 20019 8, 1972, p. 300+xiii.
[20] S.J.W (Lord) Rayleigh, The Theory of Sound, Vol. II, second ed., Dover, 1896, (1945).
[21] M.M. Zdravkovich, Comment on "Paper by Blevins (on Strohual experiments, 1984)", J. Sound Vib. 99 (2) (1985) 295–297.